

# Topological Amorphous Metals

Yan-Bin Yang, Tao Qin, Dong-Ling Deng, L.-M. Duan, and Yong Xu\*  
Center for Quantum Information, IIIS, Tsinghua University, Beijing 100084, PR China

A Weyl semimetal, a crystalline material with translational symmetry, possesses pairs of Weyl points in momentum space band structures and its topology is characterized by the first Chern number defined over a closed surface in momentum space. Here, we study amorphous systems with completely random sites and find that, through constructing and exploring a concrete model Hamiltonian, such a system can host an exotic phase of topological amorphous metal in three dimensions. In contrast to the traditional Weyl semimetals, topological amorphous metals break translational symmetry, and thus cannot be characterized by the first Chern number defined based on the momentum space band structures. Instead, their topological properties will manifest in the Bott index and the Hall conductivity as well as the surface states. Moreover, by studying the energy band and quantum transport properties, we find that topological amorphous metals exhibit a diffusive metal behavior. Our results open a door for exploring topological gapless phenomena in amorphous systems.

Weyl semimetals, three-dimensional (3D) materials with Weyl points in band structures [1–3], have attracted considerable interest [4–22] in recent years owing to their fundamental importance in mimicking Weyl fermions in particle physics and their exotic topological properties. In the context of solid-state materials, the linear energy band dispersion around a Weyl point determines the semimetal property with a zero density of states (DOS) at zero energy. In addition, the Weyl point is protected by the first Chern number defined by the integral of Berry curvatures over a closed surface in momentum space enclosing the point [23], leading to a Fermi arc consisting of surface states. This topological feature gives rise to the topological anomalous Hall effect [5, 6]. Beyond Weyl fermions that exist in particle physics, new fermions, such as type II Weyl fermions [24–26] (also called structured Weyl fermions [27]) and high spin fermions [28, 29] can appear in topological gapless materials.

All these topological gapless materials feature the existence of gapless structures in momentum space so that the topological invariants can be further defined there. Yet, this can only be guaranteed in a crystalline material with translational symmetry. Here, we ask whether a topological semimetal or metal can exist in an amorphous system with completely random sites, where the desired translational symmetry is absent. Recent development of technologies in engineering in quantum systems such as arbitrary positioning of atoms [30, 31] and in mechanical systems such as constructing interacting gyroscopes [32] have paved the way for fabricating amorphous materials. However, the study of topological phenomena in amorphous systems is still in its infancy stage and only a few works demonstrating the existence of topological insulators in amorphous systems has been reported [32–39]. Whether topological semimetals or metals exist in amorphous systems have not been explored hitherto.

In this paper, we demonstrate, by constructing and exploring a model Hamiltonian, the existence of a topological metal phase in a 3D amorphous system. The system is generated by randomly sampling sites in a box (see Fig. 1 for one sample configuration) and the results are obtained by averaging over many sample configurations. We find three distinct phases, namely, the topological amorphous metal, the amorphous An-

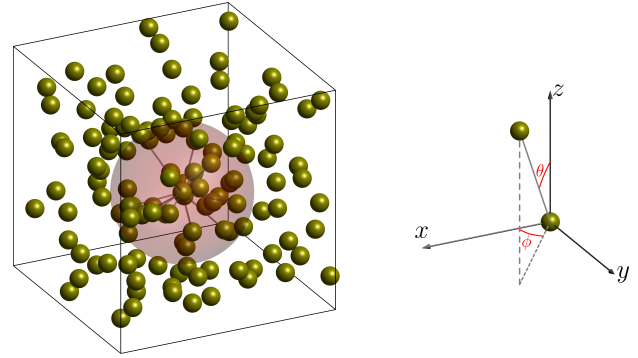


FIG. 1. (Color online) Schematic of a 3D random site configuration with the allowed hopping inside the light red sphere for a typical site at the center.

derson insulator, and the amorphous insulator phases. In contrast to Weyl semimetals with translational symmetry where their topology can be characterized by the first Chern number, the topological feature of our amorphous system is identified using the Bott index, the Hall conductivity and the surface states. To determine whether a phase in the amorphous system is a metal, a semimetal or an insulator, we compute the band properties including the energy gap, the DOS, the level statistics and the inverse participation ratio, and the transport properties including the longitudinal conductivity and the Fano factor. We find that, in the most part of the parameter region where the Bott index and the Hall conductivity are nonzero, the system is gapless, exhibiting a diffusive metal behavior. The other regions correspond to the insulating phase where the longitudinal conductivity drops to zero and the Fano factor suddenly rises to one. The insulator can be further divided into the amorphous Anderson insulator with a nonzero DOS and the amorphous insulator with a zero DOS.

**Model Hamiltonian**— We start by constructing the following model Hamiltonian

$$H = \sum_{\mathbf{x}} \left[ \sum_{\mathbf{R}} t(R) \hat{c}_{\mathbf{x}}^{\dagger} H_0(\theta, \phi) \hat{c}_{\mathbf{x}+\mathbf{R}(\theta, \phi)} + m_z \hat{c}_{\mathbf{x}}^{\dagger} \sigma_z \hat{c}_{\mathbf{x}} \right], \quad (1)$$

where  $\hat{c}_{\mathbf{x}}^\dagger = (\hat{c}_{\mathbf{x},\uparrow}^\dagger, \hat{c}_{\mathbf{x},\downarrow}^\dagger)$  with  $\hat{c}_{\mathbf{x},\sigma}^\dagger$  creating a fermion with spin  $\sigma$  at the position  $\mathbf{x}$ , which is a random vector uniformly distributed in the box,  $x_\nu \in (0, L_\nu)$  with  $\nu = x, y, z$ ,  $\mathbf{R}(\theta, \phi)$  denotes the neighboring sites as shown in Fig. 1,  $\sigma_\nu$  ( $\nu = x, y, z$ ) are the Pauli matrices and  $m_z$  is the mass term.  $H_0(\theta, \phi) = \sigma_z + i \sin \theta \cos \phi \sigma_x + i \sin \theta \sin \phi \sigma_y$  describes the hopping matrix for the neighboring sites as shown in Fig. 1. In light of irregular sites, we consider a case where the hopping strength decays exponentially  $t(R) = -e^{\lambda(1-R)}/2$ , with  $R$  being the spatial distance between two sites. Here, we have chosen the unit of energy to be dimensionless for simplicity. We take the value of  $\lambda$  so that the hopping can be neglected when  $R > R_c$ , where  $R_c$  is the longest distance with nonnegligible hopping. Here, we choose  $R_c = 2$  and the density  $\rho = N/V = 1$  where  $N$  is the number of sites and  $V = L_x L_y L_z$  is the volume of the system. For randomly distributed sets of  $\mathbf{x}$ , the system does not respect translational, time-reversal or inversion symmetries. Due to the random character, for numerical calculation, all our results are averaged over 200-600 sample configurations.

In Fig. 2(a), we map out the phase diagram with respect to the mass  $m_z$  incorporating three distinct phases (assuming the Fermi surface lies at zero energy): the topological amorphous metal, the amorphous Anderson insulator and the amorphous insulator phases, according to the Bott index (or Hall conductivity) and the band and transport properties, which will be discussed in detail in the following. For a topological phase, the Bott index is nonzero. For a diffusive metal, the energy gap is zero, the DOS and conductivity are nonzero, and the Fano factor is 1/3. For an insulator, the conductivity is zero and the Fano factor is 1. In our system, there are two types of insulators: the Anderson insulator with a nonzero DOS and the band insulator with a zero DOS.

**Bott index and Hall conductivity**— We now proceed to study the topological property of the introduced Hamiltonian. For a Weyl semimetal with translational symmetry, the topology of a gapless structure can be characterized by the topology of a closed surface in momentum space enclosing it [27]. Another signature that can be used to characterize the topology of a Weyl semimetal is the Bott index, which in 2D is equivalent to the Chern number in a crystalline system and can be harnessed to characterize the topology of a 2D Chern insulator with disorders [40] and a 2D amorphous Chern insulator [33]. The Bott index for a 3D Weyl semimetal is defined as

$$\text{Bott} = \frac{1}{2\pi L_z} \text{ImTr} \log(\tilde{U}_y \tilde{U}_x \tilde{U}_y^\dagger \tilde{U}_x^\dagger), \quad (2)$$

where  $\tilde{U}_x$  and  $\tilde{U}_y$  are the reduced matrices for  $U_x = \hat{P} e^{2\pi i \hat{x}/L_x} \hat{P}$  and  $U_y = \hat{P} e^{2\pi i \hat{y}/L_y} \hat{P}$  in the occupied space, respectively. Here,  $\hat{x}$  and  $\hat{y}$  are the position operators and  $\hat{P}$  is the projection operator for the occupied space.

The Bott index is equivalent to the topological anomalous Hall conductivity for a Weyl semimetal (see Supplementary Materials), which is not necessary to be quantized. For an amorphous system, where there is no translational symmetry,

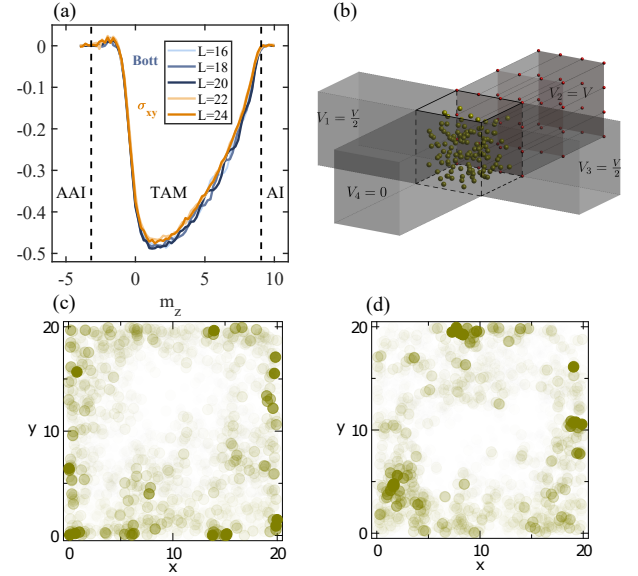


FIG. 2. (Color online) (a) The Bott index and the Hall conductivity in unit of  $e^2/(2h)$  as a function of  $m_z$  for distinct system sizes. Three different phases are identified: amorphous Anderson insulator (AAI), topological amorphous metal (TAM) and amorphous insulator (AI). (b) Schematic of a four terminal setup used to compute the Hall conductivity. (c-d) Top view of the surface states for two typical states for  $m_z = 2$  and  $m_z = 6$ , respectively. Here, the color depicts the profile of the surface states, which are clearly localized.

the momentum space band structure is not well defined as the quasimomentum is no longer a good quantum number, rendering the using of the momentum space integral to characterize its topology inapplicable. But, we can still use the Bott index. As we are interested in the case that the Fermi energy lies at zero energy, we consider the states with negative energy as the occupied space for calculating the Bott index.

In Fig. 2(a), we plot the Bott index as a function of  $m_z$  for different system sizes. Remarkably, the amorphous system exhibits nonzero values for the Bott index when  $-2.8 < m_z < 9.4$ , suggesting the topological feature of the system. Specifically, as we decrease  $m_z$  from 10, the Bott index appears from  $m_z = 9.4$  and its absolute value rises as we further decrease  $m_z$ . In this region, the Bott index exhibits several plateaus, whose location changes with respect to the system size, reflecting the finite size effect, similar to the case of a crystalline Weyl semimetal. The Bott index approaches to  $-0.49$  around  $m_z = 1.2$  and then its value sharply drops to zero and reverses with small values and finally disappears as we further decrease  $m_z$ .

To show that the Bott index reflects the Hall conductivity in a randomized system, we numerically calculate the Hall conductivity using the Landauer-Büttiker formula in a mesoscopic system. We consider four ideal leads connected to the amorphous system in the  $x$  and  $y$  directions as schematically shown in Fig. 2(b), as we expect that a surface state appears on the surfaces vertical to these directions. Under the voltage  $V_1 = V_3 = V/2$ ,  $V_2 = V$  and  $V_4 = 0$ , the Hall conductivity

is given by [41]

$$\sigma_{xy} = \frac{e^2}{2hL_z}(T_{32} - T_{34}), \quad (3)$$

where  $T_{mn}$  is the total transmission probability from lead  $n$  to  $m$ , which is computed using the nonequilibrium Green's function method [41, 42]. As  $T_{32} - T_{34}$  accounts for the contribution from chiral edge modes, for a Weyl semimetal,  $\sigma_{xy}$  is equivalent to the Bott index multiplied by  $e^2/(2h)$  and we expect that this equivalence also holds in an amorphous system.

In Fig. 2(a), we show the Hall conductivity in comparison to the Bott index. We notice the clear consistence between them in a wide range of  $m_z$  in an amorphous system as we expected. For the slight discrepancy, we estimate that it is caused by finite size effects of the Bott index, which exhibits conspicuous variations for distinct system sizes; the Hall conductivity does not show clear finite size effects when  $L = 24$  as their difference from  $L = 22$  is small (we consider a cubic case,  $L_x = L_y = L_z = L$ ). Further, the Hall conductivity does not exhibit clear plateaus from finite size effects probably due to the smearing out around the gap closing region as in Weyl semimetals. The nonzero Hall conductivity and Bott index suggest the existence of a topological amorphous phase in a wide range of parameters.

To further identify the topological feature of the system, we calculate the surface states. In light of the gapless character for an infinite system, we choose a flat-box like geometry with the height much shorter than the other two dimensions (here we take  $L_x = L_y = 20$  and  $L_z = 10$ ) so that the system is gapped under periodic boundary conditions. This enables us to pick up the surface states that are located inside the gap under open boundary conditions along the  $x$  and  $y$  directions. We illustrate the top view of the surface states in Fig. 2(c) and (d), clearly showing their localization on the boundaries.

**Band properties**— To discriminate the metal or semimetal phase from the insulator phase with respect to  $m_z$ , we compute the gap, twice of the lowest positive energy, using the Lanczos algorithm, and the DOS for large systems using the kernel polynomial method (KPM), which expands the DOS in Chebyshev polynomials to the order  $N_c$  [43]. The DOS is defined as

$$\rho(E) = \left[ \frac{1}{2N} \sum_i \delta(E - E_i) \right], \quad (4)$$

where  $E_i$  is the  $i$ th eigenvalue and [...] denotes the average over samples. Here  $\rho(E)$  is normalized to one, i.e.,  $\int dE \rho(E) = 1$ .

Figure 3(a) and (b) illustrate the gap and the DOS at zero energy  $\rho(E = 0)$  with respect to the mass  $m_z$  for distinct system sizes. Clearly, we see that the region with nonzero Bott index from  $-2.8 < m_z < 8.6$  corresponds to the gapless region: The gap for  $-3.2 < m_z < 2$  is very small even for a small system size (see the red line for  $L = 16$ ) associated with a relative large DOS.  $\rho(E = 0)$  reaches the maximum

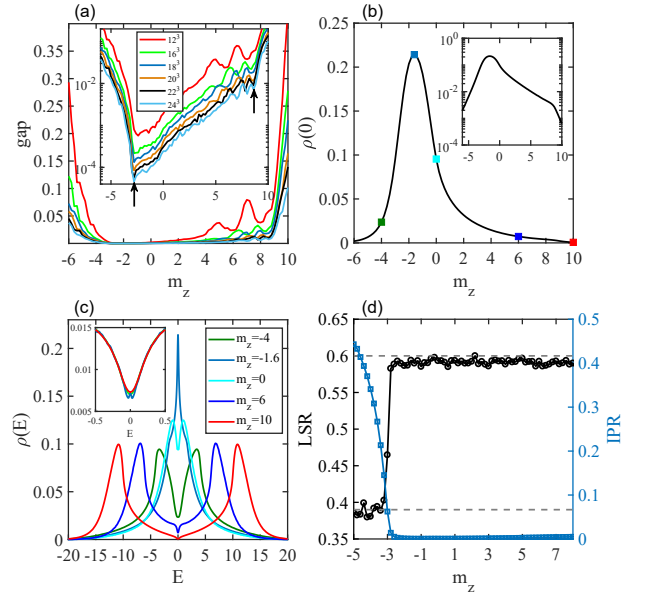


FIG. 3. (Color online) (a) The gap with respect to  $m_z$  for different system sizes calculated via the Lanczos method with the inset plotting the same thing in the logarithmic scale. The arrows show the universal dips. (b) The density of states (DOS) at zero energy  $\rho(0)$  as a function of  $m_z$  (with the logarithmic scale figure shown in the inset) calculated by the kernel polynomial method (KPM) for  $L = 55$  and  $N_c = 2^{11}$ . (c) The DOS  $\rho(E)$  versus  $E$  for various  $m_z$  in different phases for  $L = 55$  and  $N_c = 2^{11}$ . The inset plots  $\rho(E)$  versus  $E$  when  $m_z = 6$  for  $L = 55$ ,  $N_c = 2^{11}$  (red line),  $L = 60$ ,  $N_c = 2^{11}$  (green line), and  $L = 60$ ,  $N_c = 2^{13}$  (blue line). (d) The level spacing ratio (LSR)  $r(E = 0)$  (left vertical axis) and inverse participation ratio (IPR)  $I(E = 0)$  (right vertical axis) for  $L = 24$  for the states around zero energy computed via the Lanczos algorithm. In all above figures, samples in a cubic box are considered.

at  $m_z = -1.6$ , where  $\rho(E)$  versus  $E$  exhibits a steep peak at zero energy as shown in Fig. 3(c), and it decreases sharply as  $m_z$  moves away from this point associated with a developed minimum around zero energy for  $\rho(E)$  (see Fig. 3(c)). When  $2 < m_z < 8.6$ , while the energy gap strongly depends on the system size, its overall decline with increasing the system size can be observed, suggesting that this phase may be a semimetal or metal. Figure 3(b) further shows that  $\rho(E = 0)$  does not vanish in this region despite being small, implying that they correspond to a metal phase instead of a semimetal one. Specifically, for  $m_z = 6$ ,  $\rho(E)$  shows a sudden drop around zero energy (see Fig. 3(c)), but this minimum does not vanish. To exclude the finite size effect, we calculate  $\rho(E)$  using larger system size and  $N_c$  and do not find conspicuous decline of  $\rho(E = 0)$  as shown in the inset of Fig. 3(c), in stark contrast to a dramatic drop in a Weyl semimetal with quasiperiodic disorder [21].

Viewing Fig. 3(a) in the logarithmic system (see the inset), we see clearly there appears a universal dip of the energy gap for different system sizes at  $m_z = 8.6$  and  $m_z = -2.8$ . For the former,  $\rho(E = 0)$  exhibits a drop to zero there (see the

inset in Fig. 3(b)), indicating a phase transition to a band insulator (see  $\rho(E)$  versus  $E$  for  $m_z = 10$  in Fig. 3(c)). More interestingly, for the latter, the DOS does not vanish and does not show clear nonanalytic behavior with respect to  $m_z$ . This phase is actually the Anderson localized insulator (dubbed amorphous Anderson insulator), which will be identified by the level-spacing statistics, inverse participation ratio (IPR), conductivity and Fano factor.

For level statistics, we calculate the adjacent level-spacing ratio (LSR)

$$r(E) = \left[ \frac{1}{N_E - 2} \sum_i \min(\delta_i, \delta_{i+1}) / \max(\delta_i, \delta_{i+1}) \right], \quad (5)$$

where  $\delta_i = E_i - E_{i-1}$  with  $E_i$  being the  $i$ th eigenenergy sorted in an ascending order and  $\sum_i$  is the sum over an energy bin around the energy  $E$  with  $N_E$  being the energy levels counted. It is well known that for localized states,  $r \approx 0.39$  [44] associated with the Poisson statistics and for extended states,  $r \approx 0.6$  corresponding to the Gaussian unitary ensemble (GUE) [45]. In Fig. 3(d), we see that  $r(E = 0)$  is around 0.6 in the topological metal regime and drops to around 0.39 as  $m_z$  decreases from  $-2.8$ , indicating the phase transition to the localized states. Another signature we use is the real space IPR:

$$I(E) = \left[ \frac{1}{N_E} \sum_i \sum_{\mathbf{x}} (|\Psi_{E_i, \uparrow \mathbf{x}}|^2 + |\Psi_{E_i, \downarrow \mathbf{x}}|^2)^2 \right], \quad (6)$$

where  $\Psi_{E_i, \sigma \mathbf{x}}$  with  $\sigma = \uparrow, \downarrow$  are the corresponding components of the eigenstate of the system.  $I(E)$  measures how much a state around energy  $E$  is spatially localized. For a completely extended state in an infinitely large system, it is zero; for a state localized in a single site, it is one. Fig. 3(d) demonstrates that  $I(E = 0)$  is small when  $-2.8 < m_z < 8.6$  indicating that the eigenstates around zero energy are extended while it shows a steep rise across  $m_z = -2.8$ , implying the transition into the localized phase.

**Conductivity and Fano factor**— To study the quantum transport properties of amorphous systems, we compute the zero-temperature conductivity and Fano factor. Instead of connecting four leads to the system for calculation of the Hall conductivity above, we connect two ideal terminals for  $z < 0$  and  $z > L_z$  and apply periodic boundary conditions along the  $x$  and  $y$  directions to eliminate the effects of the surface states. We numerically calculate the transmission matrix  $tt^\dagger$  at zero energy by the nonequilibrium Green's function method [41, 42] and determine the zero-temperature conductance by the Landauer formula  $G = (e^2/h) \text{Tr}(tt^\dagger)$  [41] and the Fano factor  $F = \text{Tr}[tt^\dagger(1 - tt^\dagger)] / \text{Tr}(tt^\dagger)$  [8, 46].

Figure 4(a) shows the conductivity  $\sigma_{zz} = LG/W^2$  versus  $m_z$  with  $W$  and  $L$  being the width and length of the system (we here consider a cubic box geometry, i.e.,  $W = L$ ). The conductivity is nonzero in the region with nonzero Bott index from  $-2.8 < m_z < 8.6$ , showing a diffusive metal behavior as for a ballistic metal the conductivity vanishes [8].

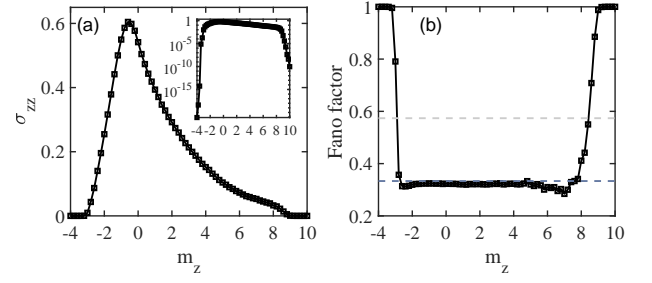


FIG. 4. (Color online) Conductivity  $\sigma_{zz}$  (a) in unit of  $e^2/h$  and Fano factor (b) versus  $m_z$  for  $L = 24$  in a cubic box. The inset plots the conductivity in the logarithmic scale, showing its steep drops across the phase transitions. The dashed lines correspond to  $F = 1/3$  and  $F = 1/3 + 1/(6 \ln 2)$ , respectively.

The conductivity drops to zero at around  $m_z = -2.8$  and at around  $m_z = 8.6$  when  $m_z$  moves away to the left and right region, respectively. The former corresponds to the transition into the Anderson insulator phase, while the latter the band insulator phase with vanishing DOS. The diffusive metal behavior is also reflected in the Fano factor that takes the value around  $F = 1/3$  [46] (see Fig. 4(b)). The transition into the insulator phase is signalled by the steep rise of the Fano factor to one due to the Poisson process. We do not find any discernible region where the Fano factor takes the value of  $F_0 = 1/3 + 1/(6 \ln 2)$  for Weyl semimetals without disorder [8], further suggesting the absence of the semimetal phase.

In summary, we have discovered a topological amorphous metal phase in 3D amorphous systems. We identify its topological feature by calculating the Bott index, the Hall conductivity and the surface states. Through further studying its band properties including the energy gap, DOS, LSR and IPR and the quantum transport properties, we find that the topological phase exhibits a diffusive metal behavior. We further predict the phase transition from the topological metal phase to the Anderson insulator phase and the band insulator phase with respect to a system parameter. Our results open a new avenue for studying topological gapless phenomena in amorphous systems. These new phenomena might be observed in various amorphous materials, such as glasses, and engineered atomic or mechanical systems.

We thank A. Agarwala, H. Jiang, S.-G. Cheng and H.-W. Liu for helpful discussions. Y.B.Y. and Y.X. are supported by the start-up fund from Tsinghua University and the National Thousand-Young-Talents Program. D.L.D. acknowledges the start-up fund from Tsinghua University. L.M.D. is supported by the Ministry of Education and the National Key Research and Development Program of China (2016YFA0301902).

\* yongxuphy@tsinghua.edu.cn

- [1] A. A. Burkov, Nat. Mater. **15**, 1145 (2016).
- [2] S. Jia, S.-Y. Xu, and M. Z. Hasan, Nat. Mater. **15**, 1140 (2016).
- [3] N. P. Armitage, E. J. Mele, and A. Vishwanath, Rev. Mod. Phys. **90**, 011001 (2018).



- 90, 015001 (2018).
- [4] X. Wan, A. M. Turner, A. Vishwanath, and S. Y. Savrasov, Phys. Rev. B **83**, 205101 (2011).
- [5] K.-Y. Yang, Y.-M. Lu, and Y. Ran, Phys. Rev. B **84**, 075129 (2011).
- [6] A. A. Burkov and L. Balents, Phys. Rev. Lett. **107**, 127205 (2011).
- [7] G. Xu, H. Weng, Z. Wang, X. Dai, and Z. Fang, Phys. Rev. Lett. **107**, 186806 (2011).
- [8] B. Sbierski, G. Pohl, E. J. Bergholtz, and P. W. Brouwer, Phys. Rev. Lett. **113**, 026602 (2014).
- [9] T. Dubček, C. J. Kennedy, L. Lu, W. Ketterle, M. Soljačić, and H. Buljan, Phys. Rev. Lett. **114**, 225301 (2015).
- [10] E. J. Bergholtz, Z. Liu, M. Trescher, R. Moessner, and M. Udagawa, Phys. Rev. Lett. **114**, 016806 (2015).
- [11] H. Weng, C. Fang, Z. Fang, B. A. Bernevig, and X. Dai, Phys. Rev. X **5**, 011029 (2015).
- [12] S. A. Yang, H. Pan, and F. Zhang, Phys. Rev. Lett. **115**, 156603 (2015).
- [13] C.-Z. Chen, J. Song, H. Jiang, Q. Sun, Z. Wang, and X. C. Xie, Phys. Rev. Lett. **115**, 246603 (2015).
- [14] S.-Y. Xu, I. Belopolski, N. Alidoust, M. Neupane, G. Bian, C. Zhang, R. Sankar, G. Chang, Z. Yuan, C.-C. Lee, S.-M. Huang, H. Zheng, J. Ma, D. S. Sanchez, B. Wang, A. Bansil, F. Chou, P. P. Shibayev, H. Lin, S. Jia, and M. Z. Hasan, Science **349**, 613 (2015).
- [15] B. Q. Lv, H. M. Weng, B. B. Fu, X. P. Wang, H. Miao, J. Ma, P. Richard, X. C. Huang, L. X. Zhao, G. F. Chen, Z. Fang, X. Dai, T. Qian, and H. Ding, Phys. Rev. X **5**, 031013 (2015).
- [16] L. Lu, Z. Wang, D. Ye, L. Ran, L. Fu, J. D. Joannopoulos, and M. Soljačić, Science **349**, 622 (2015).
- [17] Y. Zhang, D. Bulmash, P. Hosur, A. C. Potter, and A. Vishwanath, Sci. Rep. **6**, 23741 (2016).
- [18] J. H. Pixley, D. A. Huse, and S. Das Sarma, Phys. Rev. X **6**, 021042 (2016).
- [19] H. Ishizuka, T. Hayata, M. Ueda, and N. Nagaosa, Phys. Rev. Lett. **117**, 216601 (2016).
- [20] Y. Xu and L.-M. Duan, Phys. Rev. A **94**, 053619 (2016).
- [21] J. H. Pixley, J. H. Wilson, D. A. Huse, and S. Gopalakrishnan, Phys. Rev. Lett. **120**, 207604 (2018).
- [22] S. V. Syzranov and L. Radzihovsky, Annu. Rev. Cond. Mat. Phys. **9**, 35 (2018).
- [23] G. E. Volovik, *The Universe in a Helium Droplet* (Oxford University Press, Oxford, UK, 2003).
- [24] A. A. Soluyanov, D. Gresch, Z. Wang, Q. Wu, M. Troyer, X. Dai, and B. A. Bernevig, Nature **527**, 495 (2015).
- [25] K. Deng, G. Wan, P. Deng, K. Zhang, S. Ding, E. Wang, M. Yan, H. Huang, H. Zhang, Z. Xu, J. Denlinger, A. Fedorov, H. Yang, W. Duan, H. Yao, Y. Wu, S. Fan, H. Zhang, X. Chen, and S. Zhou, Nat. Phys. **12**, 1105 (2016).
- [26] L. Huang, T. M. McCormick, M. Ochi, Z. Zhao, M.-T. Suzuki, R. Arita, Y. Wu, D. Mou, H. Cao, J. Yan, N. Trivedi, and A. Kaminski, Nat. Mater. **15**, 1155 (2016).
- [27] Y. Xu, F. Zhang, and C. Zhang, Phys. Rev. Lett. **115**, 265304 (2015).
- [28] B. Bradlyn, J. Cano, Z. Wang, M. G. Vergniory, C. Felser, R. J. Cava, B. A. Bernevig, Science **353**, 6299 (2016).
- [29] B. Q. Lv, Z.-L. Feng, Q.-N. Xu, X. Gao, J.-Z. Ma, L.-Y. Kong, P. Richard, Y.-B. Huang, V. N. Strocov, C. Fang, H.-M. Weng, Y.-G. Shi, T. Qian, and H. Ding, Nature **546**, 627 (2017).
- [30] D. Barredo, S. de Léséleuc, V. Lienhard, T. Lahaye, A. Browaeys, Science **354**, 1021 (2016).
- [31] M. Endres, H. Bernien, A. Keesling, H. Levine, E. R. Anschuetz, A. Krajenbrink, C. Senko, V. Vuletic, M. Greiner, M. D. Lukin, Science **354**, 1024 (2016).
- [32] N. P. Mitchell, L. M. Nash, D. Hexner, A. M. Turner, and W. T. M. Irvine, Nat. Phys. **14**, 380 (2018).
- [33] A. Agarwala and V. B. Shenoy, Phys. Rev. Lett. **118**, 236402 (2017).
- [34] S. Mansha and Y. D. Chong, Phys. Rev. B **96**, 121405(R) (2017).
- [35] M. Xiao and S. Fan, Phys. Rev. B **96**, 100202(R) (2017).
- [36] C. Bourne and E. Prodan, J. Phys. A: Math. Theor., **51**, 235202 (2018).
- [37] K. Pöyhönen, I. Sahlberg, A. Westström, and T. Ojanen, Nat. Commun. **9**, 2103 (2018).
- [38] E. L. Minarelli, K. Pöyhönen, G. A. R. van Dalum, T. Ojanen, and L. Fritz, arXiv:1809.09578 (2018).
- [39] G.-W. Chern, arXiv:1809.10575 (2018).
- [40] T. A. Loring and M. B. Hastings, Europhys. Lett. **92**, 67004 (2010).
- [41] S. Datta, *Electronic Transport in Mesoscopic Systems* (Cambridge University Press, Cambridge, UK, 1997).
- [42] Y. Xing, Q. Sun, and J. Wang, Phys. Rev. B **75**, 075324 (2007).
- [43] A. Weiße, G. Wellein, A. Alvermann, and H. Fehske, Rev. Mod. Phys. **78**, 275 (2006).
- [44] V. Oganesyan and D. A. Huse, Phys. Rev. B **75**, 155111 (2007).
- [45] L. D'Alessio and M. Rigol, Phys. Rev. X **4**, 041048 (2014).
- [46] C. W. J. Beenakker and M. Büttiker, Phys. Rev. B **46**, 1889(R) (1992).

## SUPPLEMENTAL MATERIAL

In the supplementary material, we would like to prove the equivalence between the Bott index defined in the main text and the Hall conductivity in 3D Weyl semimetals with translational symmetry, following the method to prove its equivalence to the Chern number in 2D systems [S1]. For a Weyl semimetal, we can define the Bott index as

$$\text{Bott}_3 = \frac{1}{2\pi L_3} \text{ImTr} \log(U), \quad (\text{S1})$$

where  $U = \tilde{U}_2 \tilde{U}_1 \tilde{U}_2^\dagger \tilde{U}_1^\dagger$ ,  $U_i = P e^{2\pi i \hat{\mathbf{r}} \cdot \mathbf{a}_i / (L_i a_i)} P = \begin{pmatrix} 0 & 0 \\ 0 & \tilde{U}_i \end{pmatrix}$  with the position operator  $\hat{\mathbf{r}} = \sum_{i=1,2,3} \hat{x}_i \mathbf{a}_i$ ,  $\mathbf{a}_i$  being the lattice vectors and  $L_i$  being the size of the system along the  $\mathbf{a}_i$  direction;  $\tilde{U}_i$  is the reduced matrix in the occupied space and  $P$  is the projection operator that projects states into the occupied space. In a system with translational symmetry,  $P$  can be expressed as  $P = \sum_{n\mathbf{k}} |n\mathbf{k}\rangle \langle n\mathbf{k}|$  where  $|n\mathbf{k}\rangle$  denotes the occupied Bloch state in the  $n$ th band with the quasimomentum

$\mathbf{k} = \sum_{i=1,2,3} k_i \mathbf{G}_i / (2\pi)$ , where  $\mathbf{G}_i$  is the reciprocal lattice vector. In the coordinate representation, the Bloch state takes the form of  $\langle \mathbf{r} | n, \mathbf{k} \rangle = e^{i\mathbf{k} \cdot \mathbf{r}} u_{n,\mathbf{k}}(\mathbf{r}) = e^{i\mathbf{k} \cdot \mathbf{r}} \langle \mathbf{r} | u_{n,\mathbf{k}} \rangle$  where  $u_{n,\mathbf{k}}(\mathbf{r} + \mathbf{a}_i) = u_{n,\mathbf{k}}(\mathbf{r})$ . In this basis, we can expand  $U$  in terms of  $\delta k_i$  with  $\delta k_i = 2\pi a_i / L_i$  ( $i = 1, 2$ ),

$$U = \sum_{n_1, n_2, \dots, n_5} \sum_{\mathbf{k}} |n_1, \mathbf{k}\rangle \langle u_{n_1, \mathbf{k}} | u_{n_2, k_1, k_2 - \delta k_2, k_3} \rangle \langle u_{n_2, k_1, k_2 - \delta k_2, k_3} | u_{n_3, k_1 - \delta k_1, k_2 - \delta k_2, k_3} \rangle \langle u_{n_3, k_1 - \delta k_1, k_2 - \delta k_2, k_3} | u_{n_4, k_1 - \delta k_1, k_2, k_3} \rangle \langle u_{n_4, k_1 - \delta k_1, k_2, k_3} | u_{n_5, \mathbf{k}} \rangle \langle n_5, \mathbf{k} | \quad (S2)$$

$$= U_0 + U_2 + O(\delta k^3), \quad (S3)$$

where

$$U_0 = \sum_n \sum_{\mathbf{k}} |n\rangle \langle n|, \quad (S4)$$

$$U_2 = \sum_{n_1, n_2} \sum_{\mathbf{k}} |n_1\rangle \langle n_2| \left[ \delta k_1 \delta k_2 ((\partial_{k_2} \langle u_{n_1} |) (\partial_{k_1} | u_{n_2} \rangle) - k_1 \leftrightarrow k_2) \right. \\ \left. + \frac{1}{2} \sum_{i=1,2} \delta k_i^2 (\langle u_{n_1} | \partial_{k_i}^2 u_{n_2} \rangle + \langle \partial_{k_i}^2 u_{n_1} | u_{n_2} \rangle) \right] \\ + \sum_{n_1, n_2, n_3} \sum_{\mathbf{k}} |n_1\rangle \langle n_3| \left[ \sum_{i=1,2} \delta k_i^2 \langle u_{n_1} | \partial_{k_i} u_{n_2} \rangle \langle \partial_{k_i} u_{n_2} | u_{n_3} \rangle \right. \\ \left. + \delta k_1 \delta k_2 \langle u_{n_1} | \partial_{k_1} u_{n_2} \rangle \langle \partial_{k_2} u_{n_2} | u_{n_3} \rangle + \delta k_1 \delta k_2 \langle \partial_{k_2} u_{n_1} | u_{n_2} \rangle \langle \partial_{k_1} u_{n_2} | u_{n_3} \rangle \right], \quad (S5)$$

where  $n_i$  denotes the occupied bands, and, for briefness, we have skipped the index for  $\mathbf{k}$ . Let us further decompose  $U$  into  $U = 1 + U_{\bar{D}} + U_O$  where  $U_{\bar{D}} + 1$  denotes the diagonal part and  $U_O$  the off-diagonal one. Using this decomposition, we obtain

$$\text{Tr} \log U = \text{Tr} U_{\bar{D}} - \frac{1}{2} \text{Tr} (U_{\bar{D}} + U_O)^2 + O((U_{\bar{D}} + U_O)^3). \quad (S6)$$

Since  $U_{\bar{D}} + U_O$  is at least the second order of  $\delta k$ , the second term contributes a fourth order term and hence we neglect it. To the second order, we only need to evaluate the diagonal part, which is

$$\text{Tr} U_{\bar{D}} = \text{Tr} U_2 = \sum_n \sum_{\mathbf{k}} \left[ \delta k_1 \delta k_2 ((\partial_{k_2} u_n | \partial_{k_1} u_n \rangle - k_1 \leftrightarrow k_2) + \frac{1}{2} (\sum_{i=1,2} \delta k_i^2 \langle u_n | \partial_{k_i}^2 | u_n \rangle + c.c.) \right] \\ + \sum_n \sum_{\mathbf{k}} \sum_{n'} \sum_{i=1,2} \delta k_i^2 |\langle u_n | \partial_{k_i} u_{n'} \rangle|^2, \quad (S7)$$

where only the first term contributes to the Bott index as all other terms are purely real. Therefore, to the second order, we have

$$\text{Bott}_3 = \frac{1}{2\pi L_3} \sum_n \sum_{\mathbf{k}} \delta k_1 \delta k_2 \Omega_3(\mathbf{k}) \quad (S8)$$

$$= \frac{1}{2\pi} \sum_n \int_0^{2\pi} dk_3 C_n(k_3), \quad (S9)$$

where  $\Omega_3(\mathbf{k}) = i(\langle \partial_{k_1} u_n | \partial_{k_2} u_n \rangle - k_1 \leftrightarrow k_2)$  is the Berry curvature along the  $\mathbf{G}_3$  direction and  $C_n$  is the Chern number for a fixed  $k_3$  in the  $n$ th occupied band. Evidently, this is the Hall conductivity  $\sigma_{12}$  in unit of  $e^2/h$  and hence we prove the equivalence between the Bott index and the Hall conductivity in a Weyl semimetal.

---

\* [yongxuphy@tsinghua.edu.cn](mailto:yongxuphy@tsinghua.edu.cn)

[S1] Y. Ge and M. Rigo, Phys. Rev. A **96**, 023610 (2017).